

Bayesian parameter study of the Seyfert-starburst composite galaxies NGC 1068 and NGC 7469

Downloaded from: https://research.chalmers.se, 2026-11-09 00:29 UTC

Citation for the original published paper (version of record):
Eichmann, B., Salvatore, S., Del Palacio, S. et al (2026). Bayesian parameter study of the Seyfert-starburst composite galaxies NGC 1068 and NGC 7469. Astronomy and Astrophysics, 713. http://dx.doi.org/10.1051/0004-6361/202659464

N.B. When citing this work, cite the original published paper.

research.chalmers.se offers the possibility of retrieving research publications produced at Chalmers University of Technology. It covers all kind of research output: articles, dissertations, conference papers, reports etc. since 2004. research.chalmers.se is administrated and maintained by Chalmers Library

(article starts on next page)

A&A, 713, A208 (2026)
https://doi.org/10.1051/0004-6361/202659464
© The Authors 2026

Astronomy & Astrophysics

Bayesian parameter study of the Seyfert-starburst composite galaxies NGC 1068 and NGC 7469

B. Eichmann[1,2,⋆], S. Salvatore[1,2], S. del Palacio[3], G. Sommani[2,4], C. Mele[2,4], P. M. Veres[2,4], and J. Becker Tjus[1,2,3]

[1] Ruhr-Universität Bochum, Fakultät für Physik und Astronomie, Theoretische Physik IV, 44780 Bochum, Germany
[2] Ruhr Astroparticle and Plasma Physics Center (RAPP Center), 44780 Bochum, Germany
[3] Department of Space Earth and Environment, Chalmers University of Technology, 412 96 Gothenburg, Sweden
[4] Ruhr-Universität Bochum, Fakultät für Physik und Astronomie, Astronomisches Institut (AIRUB), 44780 Bochum, Germany

Received 16 February 2026 / Accepted 5 July 2026

ABSTRACT

Context. Multimessenger observations of the Seyfert-starburst composite galaxies NGC 1068 and NGC 7469 indicate a characteristic feature in the radio band (the so-called millimeter bump) as well as indication of high-energy neutrinos by the active galactic nucleus (AGN) corona. Moreover, the starburst ring of these sources is bright in the radio, and hence a potential source of γ-rays and neutrinos.
Aims. We aim to explain the nonthermal features of these two sources with our homogeneous steady-state Seyfert-starburst composite model, which we refined in this work. Hereby, we account for stochastic diffuse acceleration and energy losses within the corona and $\gamma\gamma$-pair attenuation of the escaping γ-rays.
Methods. Since the nonthermal features of these Seyfert sources make a minor contribution in the electromagnetic spectrum, we are left with just a few data points that can be attributed to the starburst ring or the AGN corona. Hence, a proper inclusion of the prior information on the physical parameters is needed and subsequently used in the context of a Markov chain Monte Carlo approach to avoid overfitting.
Results. Based on this Bayesian parameter study, we show that the nonthermal features of NGC 1068 can be explained well. Still a more detailed treatment of the spatial inhomogeneities in the central region of the AGN could further improve the fit results. This manifests itself even more clearly in the case of NGC 7469, where the millimeter bump needs to emerge from a coronal size of $R_c > 100\,\mathcal{R}_s$ (with the Schwarzschild radius $\mathcal{R}_s$), whereas (tera-electronvolt–peta-electronvolt)-neutrino emission requires $R_c < 10\,\mathcal{R}_s$.
Conclusions. Similar to what has previously been shown in other wave bands, our analysis highlights that the spatial extension of the so-called AGN corona depends on the considered energy of the messenger. Hence, it seems that there is not a unique edge of the corona and substantial progress in the understanding of these phenomena is expected if future analysis is to account for these spatial inhomogeneities.

Key words. neutrinos – radiation mechanisms: non-thermal – galaxies: Seyfert – galaxies: starburst

1. Introduction

Multimessenger astrophysics has significantly enlarged our understanding of the Universe. Starting with the detection of high-energy charged particles and photons across various wavelengths, an important messenger has been added about a decade ago with the observation of high-energy cosmic neutrinos (Aartsen et al. 2013).

High-energy neutrino production is typically associated with gamma-ray emission; therefore, the known diffuse gamma-ray background sets an upper limit on potential gamma-ray transparent neutrino sources. Based on this constraint, it has been shown (e.g., Murase et al. 2016) that a significant population of so-called "hidden" neutrino sources, which are opaque to giga-electronvolt–tera-electronvolt gamma rays, is necessary. A promising scenario to achieve this gamma-ray opaqueness is the presence of a bright UV/X-ray photon field close to the neutrino source to absorb giga-electronvolt–tera-electronvolt gamma rays through electron-positron pair production. For an active galactic nucleus (AGN), such a photon target is typically present very close (about some tens of Schwarzschild radii) to its central supermassive black hole in the so-called AGN corona, where X-ray photons result from Comptonization of photons emitted by the accretion disk.

Thus, high-energy neutrino sources are not necessarily γ-ray bright. But nevertheless, the IceCube Collaboration found, with a global significance of 4.2σ, a high-energy neutrino signal at tera-electronvolt energies from the direction of NGC 1068 (IceCube Collaboration 2022) based on a dedicated catalog of 110 astronomical objects that are bright in the *Fermi*-LAT energy band. Consequently, NGC 1068 is bright at giga-electronvolt gamma-rays, but tera-electronvolt gamma-rays are absent (Acciari et al. 2019). NGC 1068 is one of the closest Seyfert 2 galaxies, which is a radio-quiet type of AGN, and furthermore it hosts a circumnuclear starburst ring. Hence, the actual origin of the observed giga-electronvolt gamma-rays is unclear and a proper understanding of the high-energy signal needs to account for the broadband emission of the different kinds of messengers. To date, different groups (e.g., Inoue et al. 2020; Murase et al. 2020; Kheirandish et al. 2021; Fiorillo et al. 2024b) have proposed a model for the AGN corona to address those high-energy neutrinos. The first theoretical model that included all nonthermal emission features of NGC 1068 has

⋆ Corresponding author: eiche@tp4.rub.de

Open Access article, published by EDP Sciences, under the terms of the Creative Commons Attribution License (https://creativecommons.org/licenses/by/4.0), which permits unrestricted use, distribution, and reproduction in any medium, provided the original work is properly cited.
This article is published in open access under the Subscribe to Open model. Subscribe to A&A to support open access publication.

been provided by Eichmann et al. (2022), hereafter referred to as E+22 model. Therein, a spatially homogeneous, steady-state AGN corona and a circumnuclear starburst region are considered that are independent of each other and fueled with cosmic rays (CRs) from individual acceleration sites. It has been shown that the observational features can be nicely explained if both emission sites are taken into account. A rather large CR pressure of $\gtrsim$10% of the thermal gas pressure is needed in the AGN corona, such as was recently found by Mutie et al. (2025). Moreover, the resulting spectral behavior of the nonthermal protons has been much softer than expected from stochastic diffusive acceleration.

Most recently Sommani et al. (2025) found two IceCube real-time track alerts, out of just ∼30 per year from the direction of NGC 7469, and estimated a chance coincidence probability of 0.08% (referring to a 3.2σ significance of a detection). The spectral dependence of the neutrino flux is unclear due to the limited number of neutrinos and their energy uncertainty. Still, it seems that those neutrinos are emitted at significantly higher energies than in the case of NGC 1068. Moreover, NGC 7469 does not show any significant gamma-ray counterpart – even at giga-electronvolt or sub-giga-electronvolt energies. But as NGC 1068, NGC 7469 is also a Seyfert-starburst composite galaxy, where the circumnuclear starburst ring is responsible for most of the radio emission. However, its central AGN is classified as Seyfert 1 (or sometimes also 1.5) indicating no (or less) attenuation of the central electromagnetic emission by the dusty torus. Thus, in the case of NGC 7469 too the AGN corona constitutes the most likely origin of the potential high-energy neutrino signal. The question is whether those can be explained under consideration of the constraints given from its broadband electromagnetic emission.

In this work, we update the E+22 model and use a Bayesian approach to analyze the parameter space to explain the nonthermal multimessenger emission of NGC 1068 and NGC 7469. The paper is structured as follows: in Sect. 2, we introduce the updated Seyfert-starburst composite model, and in Sect. 3 we explain the methods used for the comparison with the observational data of NGC 1068 and NGC 7469. In Sect. 4 we show the results, before we conclude and discuss them in Sect. 5.

2. Seyfert-starburst composite model

Seyfert-starburst composite galaxies are characterized by an AGN core and a surrounding starburst environment, which can both contribute significantly to the observed nonthermal emission features. Therefore, a holistic explanation of their phenomena needs to account for both environments. Due to the large spatial scale separation, the AGN corona (on about milliparsec scales or less) and the kiloparsec-scale starburst ring can be considered as a first approximation as independent of each other. Moreover, we assumed a constant strength of the magnetic field (that is uniform on small scales and randomly orientated on significantly larger ones), as well as a thermal gas with a constant density, $n_{\rm gas}$, and temperature, $T_{\rm gas}$, in the two environments. With respect to the nonthermal emission signatures, the most relevant thermal photon targets are the UV photons from the accretion disk and the X-rays of the AGN corona, as well as the infrared (IR) emission from the re-scattered starlight by dust grains in the starburst ring (see Sect. 3 for more details). In both cases, it was assumed that these thermal fields are isotropic and stationary, even though the coronal X-ray emission often shows variability on hour and sub-hour scales. Ignoring this variability yields some inaccuracy on the coronal photon target that will be discussed further in Sect. 5.

Furthermore, the nonthermal particle population (and its resulting nonthermal emission features) was for mathematical convenience assumed to be spatially homogeneous and in a steady state.

These basic assumptions have already been used in the E+22 model, but in addition we account for the following:

(A1) In the AGN corona, the particle acceleration by stochastic acceleration (SA) occurs in the same environment as the energy losses that produce the nonthermal emission features.

(A2) In addition to a first generation of $e^{\pm}$ from hadronic processes, we included secondaries generated from leptonic radiation processes – mainly synchrotron and inverse Compton (IC).

(A3) For the AGN corona, $\gamma\gamma$-pair attenuation can also occur outside of the corona (by the anisotropic, external X-ray photons that radially leave the corona), and in addition an increased γ-ray opaqueness is possible for a shrunken γ-ray production site that does not align with the X-ray source.

To determine the momentum distribution of the relativistic electrons (i = e), positrons (i = e^+), and protons (i = p), we used the diffusion-advection equation in momentum (p) space and assume an assigned magnetic turbulence with a power spectrum of $W(k) \propto k^{-\varkappa}$ and a strength of $\eta^{-1} \equiv 8\pi \int W(k)\,{\rm d}k/B^2$, adopting Kolmogorov turbulence ($\varkappa = 5/3$) in the following. Furthermore, we incorporated the impact of continuous momentum losses ($\langle \dot{p} \rangle < 0$) by interactions with, for example, ambient gas and photon targets, as well as catastrophic losses on a momentum-dependent timescale, $t_{\rm esc}(p)$, such as by escape from the physical system[1]. When the turbulent magnetic field is small compared to the regular magnetic field ($\eta^{-1} < 1$), the steady-state transport equation for the differential CR particle density, $n_i(p) = 4\pi\, p^2\, \langle f(p) \rangle$, in this region becomes

$$-\frac{\partial}{\partial p}\left[p^2\, D(p) \frac{\partial}{\partial p}\left(\frac{n_i}{p^2}\right)\right] \tag{1}$$

$$+\frac{\partial}{\partial p}\left(\langle \dot{p} \rangle n_i\right) + \frac{n_i}{t_{\rm esc}(p)} = \begin{cases} q_{\rm p}(p) & \text{for} \quad i = {\rm p} \\ q_{\rm e}(p) + q_{\rm e^{\pm}}^{\rm 2nd}(p) & \text{for} \quad i = {\rm e} \end{cases}, \tag{2}$$

where $D(p) \propto p^{\varkappa}$ is the momentum diffusion coefficient, describing the interaction rate with the magnetic turbulence. Thus, the coronal condition (A1) is represented by both lines (1 + 2) of the previous equation. However, the first term (1) can be neglected for the starburst environment where SA is typically subdominant as particles are more likely accelerated by supernova remnants (SNRs) via diffusive shock acceleration (DSA), which can be treated in a mathematically convenient way by a primary source rate, $q_i(p)$. Therefore, we used the same transport equation with a two-zone approach as in the E+22 model for the starburst ring. Hence, we adopted

$$q_i(p) = \begin{cases} q_{0,i}\,(p/p_0)^s\, \exp(-p/\hat{p}_i) & \text{for the starburst,} \\ q_{0,i}\,\delta(p/p_{{\rm inj},i} - 1) & \text{for the AGN corona,} \end{cases} \tag{3}$$

[1] All details on the energy losses, the escape, and the acceleration timescales can be found in E+22. Note that the diffusive behavior in the nonrelativistic particle regime changes, as (i) the diffusion coefficients reduces due to lower particle velocities, and (ii) different resonances with the magnetic turbulence occur, leading typically to longer escape times compared to relativistic particles at comparable energies. Hence, particle escape is insignificant and the nonrelativistic particles will predominantly suffer from continuous momentum losses if acceleration is not at work.

where either already accelerated particles up to a maximal momentum, $\hat{p}_i$, are injected into the starburst environment, or super-thermal particles enter the coronal environment with a distinct momentum, $p_{\mathrm{inj},i}$, specified by the velocity of the turbulent modes that subsequently accelerate these particles within the environment. Hereby, we adopted physical parameters in the vicinity of the SNRs that are similar to what is found in the whole starburst environment, so that $\hat{p}_i$ was determined by the equilibrium of the characteristic acceleration and loss timescale in the starburst ring. In the case of the AGN corona, we assumed that a resonant interaction with the magnetosonic-type turbulence is only possible for suprathermal particles whose velocity is comparable to the velocity of the fast magnetosonic mode – which is about the Alvfén speed, v_{A}, for low a plasma beta or magnetically dominated plasma. This condition sets the low-energy cutoff of the momentum diffusion coefficient, and therefore, $p_{\mathrm{inj},i} = p(v_{\mathrm{A}})$.

The normalization, $q_{0,\mathrm{p}}$, of the CR proton injection rate was determined as follows:

(i) For the AGN corona, we adopted that a certain fraction, f_{gas}, of the thermal gas pressure is transferred to CRs, i.e.,

$$f_{\mathrm{gas}} = \frac{c \int \mathrm{d}p\, n_{\mathrm{p}}(p)\, p/3}{k_{\mathrm{B}}\, n_{\mathrm{gas}}\, T_{\mathrm{gas}}},$$

where $T_{\mathrm{gas}} = m_{\mathrm{p}} c^2/(6 r_{\mathrm{c}} k_{\mathrm{B}})$ denotes the virial temperature[2] of the protons and k_{B} is the Boltzmann constant. Here, the coronal region is constrained to a radius of $R_{\mathrm{c}} = r_{\mathrm{c}} \mathcal{R}_{\mathrm{s}}$, where $\mathcal{R}_{\mathrm{s}} = 2GM/c^2$ denotes the Schwarzschild radius of the supermassive black hole with mass M.

(ii) For the starburst ring, a fraction, f_{SN}, of the total SN energy is transferred to CRs, so that

$$f_{\mathrm{SN}} = \frac{V^{\mathrm{s}}_{\mathrm{geo}}\, c \int \mathrm{d}p\, q_{\mathrm{p}}(p)}{E_{\mathrm{SN}}\, \tau^{-1}_{\mathrm{SN}}},$$

where a typical total SN energy of $E_{\mathrm{SN}} = 10^{51}$ erg, as well as a SN rate of Veilleux et al. (2005), $\tau^{-1}_{\mathrm{SN}}(\mathrm{NGC\,1068}) = 0.51\,\mathrm{yr}^{-1}$, and Laine et al. (2006), $\tau^{-1}_{\mathrm{SN}}(\mathrm{NGC\,7469}) = 0.33\,\mathrm{yr}^{-1}$, respectively, is used. Moreover, the volumes of the starburst ring of the considered sources are $V^{\mathrm{s}}_{\mathrm{geo}}(\mathrm{NGC\,1068}) = 3.47\,\mathrm{kpc}^3$ for an adopted outer radius of $R^{\mathrm{s}}_{\mathrm{out}} = 1.5\,\mathrm{kpc}$ and $V^{\mathrm{s}}_{\mathrm{geo}}(\mathrm{NGC\,7469}) = 1.57\,\mathrm{kpc}^3$ using $R^{\mathrm{s}}_{\mathrm{out}} = 1\,\mathrm{kpc}$, respectively.

Based on these proton normalizations, we adopted a quasi-neutral accelerator above a characteristic minimal velocity[3]: In the case of the starburst ring, we applied $\int_{p_{\mathrm{sh,p}}}^{\infty} \mathrm{d}p\, q_{\mathrm{p}}(p) = \int_{p_{\mathrm{sh,e}}}^{\infty} \mathrm{d}p\, q_{\mathrm{e}}(p)$ above the average kinetic energy of the shock front of about 10 keV, which is well motivated by simulations (Caprioli et al. 2014) and observations (Morlino & Caprioli 2012). For the AGN corona, where acceleration is explicitly taken into account by the transport Equation ((1) + (2)), this assumption yields $\int_{p_{\mathrm{inj,p}}}^{\infty} \mathrm{d}p\, n_{\mathrm{p}}(p) = \int_{p_{\mathrm{sh,e}}}^{\infty} \mathrm{d}p\, n_{\mathrm{e}}(p)$. Note that the final fit results indicate that the primary electron population plays only an insignificant role (see Fig. 1) in the nonthermal emission features, so that other assumptions on its normalization can also be applied without affecting our results.

In addition, the mostly dominating leptonic source term $q^{\mathrm{2nd}}_{\mathrm{e}^{\pm}}(p)$ refers to the injection rate of secondary electrons, e^-, and positrons, e^+, which is treated more accurately than in the E+22 model according to (A2). These secondaries can emerge either from hadronic processes directly or, for the AGN corona, from $\gamma\gamma$-pair attenuation. In the latter case, the γ-ray emission can also result from leptonic processes, such as IC scattering, leading to a nonlinear dependency in the transport equation. To break this nonlinearity, we employed an iterative approach, whereby leptonic γ-rays as well as the resulting pairs from $\gamma\gamma$-pair attenuation were calculated for each generation of the secondaries until the additional contribution became negligible. Finally, the hadronic contribution as well as the different leptonic contributions were summed up, yielding the total source rate, $q^{\mathrm{2nd}}_{\mathrm{e}^{\pm}}(p)$.

The general solution of the steady-state momentum diffusion Equation ((1) + (2)) has been provided by Walter & Eichmann (2025). This leads to a significantly harder momentum distribution in the AGN corona than for the case of the simplified Eq. (2) that has been used in E+22. Using the best-fit parameters (see Sect. 4.1 for more details), the left panel in Fig. 1 illustrates these hard spectra for the CR protons (red line), whereas primary CR electrons do not reach such energies due to dominant Coulomb losses at low energies. Therefore, secondary electrons (solid blue line), which emerge predominantly from hadronic interaction processes, constitute the distribution function at high energies. Here, we do not account for SA, which is typically inefficient due to strong synchrotron and IC cooling. For the starburst ring (right panel in Fig. 1), DSA is expected to yield significantly softer injection spectra than SA, which becomes even softer within the starburst ring in the case of CR electrons due to synchrotron and IC cooling. Also in this environment the high-energy electrons emerge – for the considered best-fit scenario – predominantly from hadronic interaction processes.

Based on the resulting CR distribution function, $n_i(p)$, we can determine the resulting nonthermal photon and neutrino flux for the individual emission sites, such as in E+22. But in addition to the internal attenuation by the isotropic X-ray photon target within the AGN corona, we also accounted for the external attenuation (A3) as follows.

As shown in E+22 (and references therein), the internal attenuation can be associated with an attenuation factor, $f^{\mathrm{int}}_{\mathrm{att}} = V_{\mathrm{eff}}(\tau)/V_{\mathrm{geo}}$, which is given by the ratio of the effective volume,

$$V^{\mathrm{c}}_{\mathrm{eff}}(\tau) = \frac{\pi R^3_{\mathrm{c}}}{\tau}\left[1 + \frac{(2\tau+1)\exp(-2\tau) - 1}{2\tau^2}\right], \tag{4}$$

over the geometrical volume, $V^{\mathrm{c}}_{\mathrm{geo}} = 4\pi R^3_{\mathrm{c}}/3$, yielding $f^{\mathrm{int}}_{\mathrm{att}} \propto \tau^{-1}$ for an optical depth of $\tau \gg 1$. Note that this relation only holds for a homogeneous spherical symmetric system with constant emission and absorption coefficients.

However, this is no longer the case for the external attenuation, where the emission coefficient vanishes since gamma-rays are only produced inside of the AGN corona. Therefore, the external attenuation factor is provided by $f^{\mathrm{ext}}_{\mathrm{att}} = \exp(-\tau)$, where the optical depth, τ, accounts for the radially decreasing target photon density. The differential external X-ray target photon number, $\mathrm{d}N_{\mathrm{X}}$, per frequency, $\mathrm{d}\nu$, volume, $\mathrm{d}V$, and solid angle, $d\Omega = 2\pi\, d\mu$, at a distance, x, from the center of the corona is

[2] Note that the AGN corona resides in the deep gravitational potential of the black hole, where dissipative processes heat the plasma until its thermal energy is comparable to its gravitational binding energy, as expected from the virial theorem. Hence, the virial temperature sets the characteristic temperature of the ions (protons), which dominate the gravitational energy budget.

[3] Due to their different rest masses, electrons and protons attain different minimum injection momenta, which enables them to participate in the acceleration process to normalize the primary CR electrons.

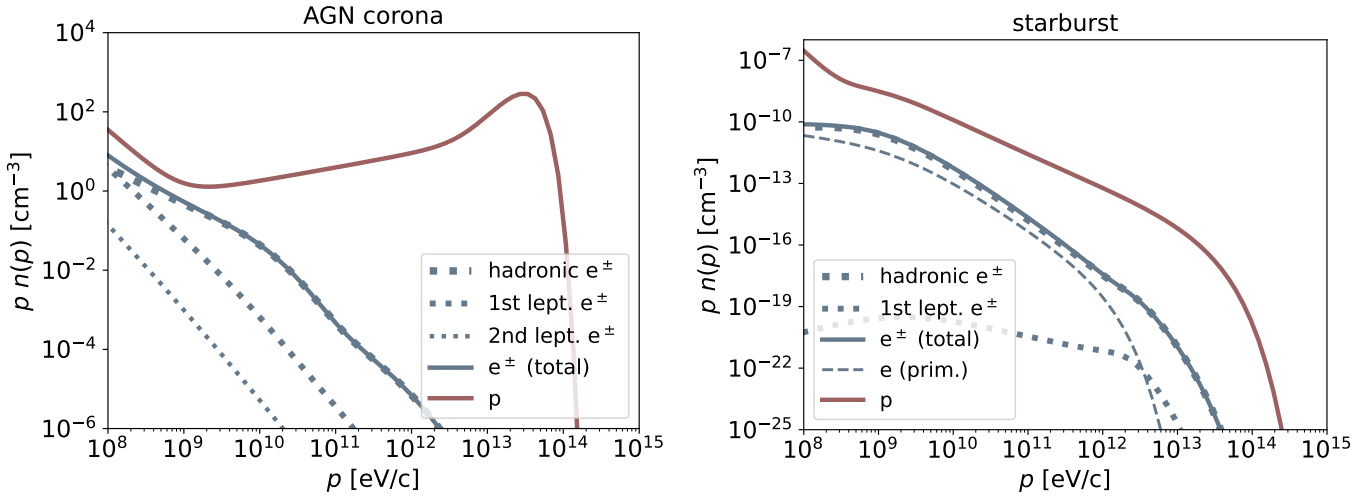


Fig. 1. Best-fit model predictions of the CR electron (blue) and proton (red) distribution within the AGN corona (*left*) and the starburst-ring (*right*) of NGC 1068.

given by

$$n_{\rm X}^{\rm ext}(\nu,\, x,\, \mu) \equiv \frac{1}{2\pi}\,\frac{{\rm d}N_{\rm X}}{{\rm d}\nu\,{\rm d}V\,{\rm d}\mu'}\left|\frac{{\rm d}\mu'}{{\rm d}\mu}\right| = \frac{L_\nu}{2\pi\,R_{\rm c}^2 c\,h\nu}\left(\frac{R_{\rm c}}{x}\right)^2\left|\frac{{\rm d}\mu'}{{\rm d}\mu}\right|, \tag{5}$$

where μ denotes the cosine of the interaction angle at a certain distance, x, from the center of the system and μ' is at $x = 0$ the cosine of the angle between the line of sight and the position on the surface of the corona, where the interacting X-ray escapes the system. The calculation of the Jacobian determinant yields the physically relevant solution[4]

$$\left|\frac{{\rm d}\mu'}{{\rm d}\mu}\right| = \left|-\frac{2x}{R_{\rm c}}\mu + \frac{\left(\frac{2}{R_{\rm c}}\right)^2\left[4\mu^3 - 2\mu\right] + 2\mu}{2\sqrt{\left(\frac{x}{R_{\rm c}}\right)^2\left[\mu^4 - \mu^2\right] + \mu^2}}\right|. \tag{6}$$

Hereby, we set the photon target to be isotropic within the corona, i.e., no dependence on μ', and photons are leaving the surface isotropically, so that $n_{\rm X}^{\rm ext}$ depends on the cosine of the interaction angle, μ (between the X-ray and the gamma-ray), at a distance of $x > R_{\rm c}$. Using this photon target, the external optical depth due to $\gamma\gamma$-pair attenuation for a gamma-ray with an energy, E_γ, is given by (Breit & Wheeler 1934; Heitler 1954)

$$\tau_{\gamma\gamma}^{\rm ext}(E_\gamma) = 2\pi\int_{-1}^{1}{\rm d}\mu\,(1-\mu)\int_{R_{\rm c}}^{d}{\rm d}x\int_{\nu_{\rm th}}^{\infty}{\rm d}\nu\, n_{\rm X}^{\rm ext}(\nu,x,\mu)\,\sigma_{\gamma\gamma}(E_\gamma,\nu,\mu), \tag{7}$$

with the pair production threshold frequency

$$\nu_{\rm th} = \frac{2m_e^2c^4}{h\,E_\gamma(1-\mu)}, \tag{8}$$

the cross section

$$\sigma_{\gamma\gamma}(E_\gamma,\nu,\mu) = \frac{3\sigma_{\rm T}}{16}\left(1-\beta^2\right)\left[\left(3-\beta^4\right)\ln\left(\frac{1+\beta}{1-\beta}\right) - 2\beta\left(2-\beta^2\right)\right], \tag{9}$$

and the dimensionless center-of-momentum velocity

$$\beta(E_\gamma,\nu,\mu) = \sqrt{1 - \frac{2m_e^2c^4}{\nu h\,E_\gamma(1-\mu)}}. \tag{10}$$

Moreover, we also address a scenario in which the gamma-ray emission region is completely confined within the corona at a radius of $(1 - r_{\rm sh})R_{\rm c}$, such that there is an outer shell containing only X-ray emitting coronal plasma, similar to what has previously been discussed by Inoue et al. (2020). In this case, the attenuation is also given by $f_{\rm att}^{\rm sh} = \exp(-\tau)$ due to the adopted absence of gamma-ray sources within the outer spherical shell between $(1 - r_{\rm sh})R_{\rm c}$ and $R_{\rm c}$, where $r_{\rm sh} < 1$ denotes the thickness of this shell in units of $R_{\rm c}$. But in contrast to the previous case of external attenuation, the target-photon distribution is still isotropic and constant within this shell, leading to a much higher absorption probability.

The spectral energy flux of the messenger type, $m \in \{\gamma, \nu\}$, for a homogeneous source with a constant emission coefficient, ϵ_m, and an absorption coefficient, α_m, at a distance, d, is given by (e.g., Gould 1979)

$$F_m(E_m) = \frac{E_m}{4\pi\,d^2}\,\epsilon_m(E_m)\,V_{\rm eff}(E_m), \tag{11}$$

with the effective emission volume

$$V_{\rm eff}(E_m) = \int {\rm d}^3r\,\exp\left(-\alpha_m(E_m)\,|\boldsymbol{r}_{\rm s} - \boldsymbol{r}|\right), \tag{12}$$

where $\boldsymbol{r}_{\rm s}$ represents an arbitrary position on the surface of the emission volume (see E+22 for more details on ϵ_m and α_m). Since the considered sources are at a distance of <100 Mpc and $E_\gamma < 10$ TeV, the γ-attenuation by the extragalactic background light is negligible.

3. Methods

In the following, we apply our model to explain the nonthermal observational data from NGC 1068 and NGC 7469. However, the nonthermal phenomena that can be attributed to their starburst ring or the AGN corona only emerge at the radio[5]- and

[4] Note that the other mathematical solution, where the second term is subtracted, is not relevant for the considered scenario of photons that are isotropically leaving the coronal surface.

[5] Note that at radio/mm wavelengths, the emission can be a combination of thermal and nonthermal radiation.

gamma-ray (only for NGC 1068) band as well as at about tera-electronvolt–peta-electronvolt energies for the neutrinos. Hence, this lack of fit data demands a consideration of prior information on the model parameters to avoid overfitting. For the majority of parameters, a truncated normal distribution (mostly in log-space) was applied, where minimal or maximal values represent limits that result either from fundamental physical constraints or observational certainty. The standard deviation, σ, describes the adopted confidence on the expectation, μ. Only for r_c, there is no expectation (but a clear minimal and maximal value), so that a uniform distribution is used (see Table 1).

To describe the γ-ray flux from NGC 1068 and NGC 7469, we need to account for the coronal target photon field, which can be estimated from the characteristic X-ray flux at these energies. In the case of NGC 7469, the impact of the torus attenuation is assumed to be negligible and the spectral distribution from Mehdipour et al. (2018) with a coronal X-ray luminosity (between 2 and 10 keV) of $L_X = 1.7 \times 10^{43}$ erg/s is used to model the intrinsic target field. Hereby, *Chandra*-HETGS, *HST*-COS, and *Swift*-UVOT data from 2015 were fitted, yielding an X-ray flux that is just slightly larger than the results from previous epochs.

However, for the Seyfert 2 galaxy NGC 1068 a more detailed modeling of the impact of the torus is necessary to obtain the intrinsic coronal target photon field. NuSTAR and XMM-Newton monitoring campaigns (Marinucci et al. 2016) yield an intrinsic luminosity of $L_X = 7^{+7}_{-4} \times 10^{43}$ erg/s between (2−10) keV, which is used in the following. Consequently, the black hole mass of NGC 1068 was estimated to be $M_{BH} = 1.7 \times 10^7\, M_\odot$ (e.g., GRAVITY Collaboration 2020), which leads to an Eddington luminosity of $L_{Edd} = 2.1 \times 10^{45}$ erg s^{-1}. Moreover, the empirical relation of Hopkins et al. (2007) was used to determine L_{bol} based on L_X. Finally, the resulting Eddington ratio, $\lambda_{Edd} = L_{bol}/L_{Edd}$, was used to model the spectral behavior of the X-ray corona field by a power law, with a photon index of $\Gamma_X \simeq 2 + 0.167 \log(\lambda_{Edd})$ (see Trakhtenbrot et al. 2017) and an exponential cutoff at (Ricci et al. 2018) $E_{X,cut} \simeq [-74 \log(\lambda_{Edd}) + 1.5 \times 10^2]$ keV. Moreover, the parametrized model by Ho (2008) was used between 2 eV and 2 keV for the thermal UV photon spectrum from the disk.

In addition to these coronal X-ray fields, the AGNs present extended diffuse emission produced on significantly larger scales, whose physical origin remains ambiguous. This extended emission can be dominant within the radio and IR bands (depending on the angular resolution of the observations). Here we stay agnostic to this extended component and use the approach from Mutie et al. (2025) where, in addition to the non-thermal coronal contribution, three components from the vicinity of the AGN are taken into account:

(i) An extended synchrotron contribution by diffuse CR electrons, which may be related to the jet, and which emits a spectrum according to

$$S_{sy}(\nu) = A_{sy} \left(\frac{\nu}{\nu_0}\right)^{\alpha_{sy}} . \tag{13}$$

(ii) Free–free radiation by the ionized gas, which extends beyond the spatial scales of the X-ray corona, and whose optical thin spectrum is given by

$$S_{ff}(\nu) = A_{ff} \left(\frac{\nu}{\nu_0}\right)^{\alpha_{ff}} . \tag{14}$$

(iii) Thermal emission from the dust particles within the unresolved core (i.e., at a radial distance $\lesssim$1 pc and $\lesssim$100 pc from the core of NGC 1068 and NGC 7469, respectively) that can be modeled as a modified-blackbody spectrum yielding

$$S_d(\nu) = A_d \left(\frac{\nu}{\nu_0}\right)^2 (1 - \exp[-(\nu/\nu_{\tau_1})^{\beta_d}]) , \tag{15}$$

where $\nu_{\tau_1} \sim 800$ GHz is the frequency at which the dust becomes optically thick and $\beta_d \sim 1.5$–2 is related to the dust opacity law. In general, the diffuse synchrotron component (i) is dominant at low frequencies, then free–free becomes more relevant, and at high frequencies (submillimeter to FIR regime) the dust dominates. In some sources – including NGC 1068 and NGC 7469 – the spectral energy distribution (SED) shows an additional bump around millimeter wavelengths that is associated with emission from the compact corona. For NGC 1068, Mutie et al. (2025) showed that component (i) has a negligible impact on the explanation of this millimeter bump. Therefore, only free–free and thermal dust emission is taken into account. For NGC 7469 a similar MCMC analysis was performed (del Palacio et al., in preparation), yielding an extended synchrotron contribution that becomes relevant at frequencies of $\lesssim$100 GHz, so this component was also taken into account. All details on the adopted parameters for these fixed contributions from the vicinity of the AGN are given in Table 2.

Taking into consideration these fixed components, we fit the extended and compact radio emission, as well as the γ-ray and neutrino data (in case of NGC 7469 only γ-ray upper limits are available) from these two Seyfert-starburst-composite galaxies (see Tables 3 and 4). Hereby, the standard sampler for Markov chain Monte Carlo `EMCEE` (Foreman-Mackey et al. 2013) was used, where for a given set of model parameters (θ) under consideration of the previously mentioned radio and high-energy data (D), the posterior probability density function $P(\theta|D) \propto \exp[-\chi^2(\theta)/2]\,\Pi(\theta)$ was computed. Here, $\Pi(\theta)$ denotes the priors adopted for each parameter (see Table 1 for more details), and the likelihood depends on $\chi^2(\theta) = \sum_i (F_i(\theta) - F_{D,i})^2/(\Delta F_{D,i})^2$, where $F_i(\theta)$ refers to the predicted flux (11) and $F_{D,i}$ and $\Delta F_{D,i}$ denote the observed flux and its uncertainty, respectively, for a certain messenger at a certain energy (i). Note, that the relative uncertainty, $\Delta F_{D,i}/F_{D,i}$, of some of the ALMA data (cor) is multiple orders of magnitude smaller than what is given at high energies, so that the likelihood would become completely dominated by these data points. In order to avoid such behavior and to address the additional uncertainty that results from the limited spatial resolution as well as the limited accuracy of our model prediction, we use in the following a minimal uncertainty of $\Delta F_{D,i} \geq 0.15\, F_{D,i}$ unless otherwise stated. In the case of NGC 7469, the nonthermal flux prediction of the starburst ring does not depend significantly on the coronal contribution, if we assume that the high-energy neutrinos need to emerge from the AGN corona. Hence, we performed two independent MCMC fits for these two environments of NGC 7469 due to computational efficiency. The fixed extended AGN emission of NGC 7469 can become dominant at 1.4 GHz, if free-free absorption is negligible at these frequencies. However, the free-free optical depth, τ_{ff}(1.4 GHz), strongly depends on the details of the gas distribution within this extended region. Therefore, the given flux at this frequency rather serves as an upper limit for the flux contribution of the starburst ring. Hence, we artificially increased the relative inferior data uncertainty of the low resolution flux at 1.4 GHz to 100% in the likelihood of the MCMC.

Table 1. Prior distributions $\Pi(\theta)$ used for model parameters θ of starburst ring (str) and AGN corona (cor).

Parameter (θ)	Env.	Prior parameters	Note
$\ln(\eta_c^{-1})$	cor	$\mu = \ln(0.1)$, $\sigma = \ln(10)$, $\ln(\eta_c^{-1}) < \ln(0.9)$	turbulence strength[a)]
$\ln(f_{gas})$	cor	$\mu = \ln(0.1)$, $\sigma = \ln(100)$, $\ln(f_{gas}) < \ln(1)$	gas-to-CR pressure ratio[b)]
$\ln(\beta_B)$	cor	$\mu = \ln(0.5)$, $\sigma = \ln(10)$, $\ln(0.05) < \ln(\beta_B) < \ln(5)$	plasma beta[c)]
$\ln(\omega_T)$	cor	$\mu = \ln(0.5)$, $\sigma = \ln(10)$, $\ln(0.05) < \ln(\omega_T) < \ln(5)$	optical Thomson depth[d)]
r_c	cor	$r_c \in [1, 1000]$	coronal radius
$\ln(\eta_s^{-1})$	str	$\mu = \ln(0.1)$, $\sigma = \ln(10)$, $\ln(\eta_s^{-1}) < \ln(0.9)$	turbulence strength[a)]
$\ln(f_{SN})$	str	$\mu = \ln(0.1)$, $\sigma = \ln(100)$, $\ln(f_{SN}) < \ln(0.5)$	SN-to-CR energy ratio[e)]
$\ln(B_s/1\,\mu G)$	str	$\mu = \ln(100)$, $\sigma = \ln(3)$, $\ln(10) < \ln(B_s/1\,\mu G) < \ln(1000)$	av. magnetic field strength[f)]
$\ln(n_{gas}/1\,cm^{-3})$	str	$\mu = \ln(500)$, $\sigma = \ln(5)$, $\ln(50) < \ln(n_{gas}/1\,cm^{-3}) < \ln(5000)$	av. gas density[g)]
s	str	$\mu = -2.25$, $\sigma = 0.5$, $-1.5 > s > -2.5$	source rate spectral index[h)]

Notes. More details on the motivation for the parameter expectation can be found here: [a)] e.g., Fiorillo et al. (2024a) for the AGN corona and Beck (2012) for the starburst. In principle also larger μ values can be expected, that however, leads to inconsistency with the adopted quasilinear approximation in Eq. ((1) + (2)). [b)] Petrosian & Liu (2004). [c)] Jiang et al. (2019, 2014); Miller & Stone (2000). [d)] Ricci et al. (2018); Merloni & Fabian (2001). [e)] E.g., Haggerty & Caprioli (2020), where the normalized CR pressure quickly converges toward about 10%. Additional uncertainty results from the adopted typical SN energy of 10^{51} erg. [f)] E.g., Thompson et al. (2006). [g)] E.g., Hsieh et al. (2011); García-Burillo et al. (2014); Izumi et al. (2015). [h)] Based on the nonlinear DSA scenario and source-to-source variations inferred in cosmic-ray population studies (e.g., Blasi & Amato 2012; Yuan et al. 2011; Strong et al. 2007).

Table 2. Fixed radio parameters for NGC 1068 and NGC 7469.

Parameter	NGC 1068	NGC 7469
ν_0 [GHz]	100	100
A_{sy} [Jy]	–	0.50
α_{sy}	–	−1.33
A_{ff} [Jy]	10.47	1.34
α_{ff}	−0.1	−0.1
A_d [Jy]	0.022	1.585
ν_{τ_1} [GHz]	800	820
β_d	2	1.78

3.1. New data acquisition

Most of the data that is used in the MCMC fit has already been published as indicated in Tables 3 and 4. But in the case of NGC 1068 we reinvestigated the large-scale radio emission from the starburst ring. Due to the nonvanishing radio contribution by the jet of NGC 1068, which is not taken into account in this work, we need to ensure that the chosen spatial scales of the large-scale radio data exclude the jet contribution. Therefore, we used the publicly available map from the FIRST survey (White et al. 1997) at 1.43 GHz, which provides a total flux from the whole ∼25″ aperture of 4.41 ± 0.01 Jy. Guided by a higher-resolution map at 4.8 GHz, we identified the jet contribution, and consequently removed the flux coming from an ellipse of ∼13″ × 9″, leading to 1.43 GHz flux by the starburst ring of 0.3 ± 0.1 Jy. Hereby, we used a conservative estimate on the uncertainty that includes the uncertainty of the chosen size. Hence, about 7% of the total flux at 1.43 GHz emerges from the starburst ring, which is about a factor of three less than what has been used in E+22 but in good agreement with a previous analysis by Mutie (2019). Using the large-scale spectral behavior from Wynn-Williams et al. (1985) with $S_\nu \propto \nu^{\alpha_\nu}$, where $\alpha_\nu = -0.8\,(-1)$ between 20 and 6 cm (between 6 and 2 cm), we estimated the flux at 5 GHz and 15 GHz – see Table 3. Hereby, we adopted a spectral uncertainty of $\Delta\alpha_\nu = 0.05$.

In the case of NGC 7469, there is no significant jet contribution, so that all components of the large-scale radio emission are considered in our model. Using the VLA *L*-Band A-array data from Project ID: 23A-324 obtained through the NRAO archive, we obtain a total flux at 1.5 GHz of 0.18 ± 0.00054 Jy from an aperture of ∼1.43″ × 0.82″. The flux was estimated using a single-component Gaussian on the source, with the uncertainty of the flux estimated using the root mean square noise.

At higher energies, we used ∼15.5 years of *Fermi*-LAT (Atwood et al. 2009) data[6] (from 4 August 2008 to 1 January 2024) between 100 MeV and 1 TeV. We selected a region of interest (ROI) of 15° centered on the optical position of NGC 7469 and Pass 8 SOURCE class events (evclass = 128). A zenith angle cut of 90° was applied. The analysis was performed using the P8R3 SOURCE V3 instrument response functions (Bruel et al. 2018), together with the most recent Galactic (`gll_iem_v07`) and isotropic diffuse emission (`iso_P8R3_SOURCE_V3_v1`) models, and the *Fermi*-LAT 4FGL DR4 source catalog (Abdollahi et al. 2020). The LAT data were reduced with FERMIPY (Wood et al. 2017), following the standard analysis procedure. This included optimizing the ROI, freeing and fitting the normalizations of sources within 2° of the target, and performing a global likelihood fit. We subsequently added a trial point source at the position of the Seyfert galaxy and repeated the likelihood analysis. To assess the presence of γ-ray emission from NGC 7469 over the full 15.5-yr *Fermi*-LAT dataset, we generated test statistic (TS) maps and evaluated the TS value at the source position. We obtained a TS value consistent with zero, indicating that NGC 7469 is not detected by *Fermi*-LAT. This result is consistent with the absence of the source in the FGL catalogs, and rules out even a marginal detection. Hereby, the `sed()` method of FERMIPY was applied to determine 95% CL spectral upper limits – see Table 4.

4. Results

In general we noticed that the coronal radio prediction is strongly constraint by the given millimeter data, despite the additional

[6] https://fermi.gsfc.nasa.gov/cgi-bin/ssc/LAT/LATDataQuery.cgi

Table 3. Fit data for NGC 1068.

Env.	Energy [eV]	Flux [eV s^{-1} cm^{-2}]
str[a)]	0.6×10^{-5}	$(7 \pm 2) \times 10^{-3}$
str[a)]	2.1×10^{-5}	$(10 \pm 3) \times 10^{-3}$
str[a)]	6.2×10^{-5}	$(10 \pm 3) \times 10^{-3}$
cor[b)]	0.78×10^{-4}	$(0.153 \pm 0.001) \times 10^{-2}$
cor[b)]	0.80×10^{-4}	$(0.153 \pm 0.001) \times 10^{-2}$
cor[b)]	0.82×10^{-4}	$(0.155 \pm 0.001) \times 10^{-2}$
cor[b)]	0.91×10^{-4}	$(0.165 \pm 0.001) \times 10^{-2}$
cor[b)]	0.92×10^{-4}	$(0.174 \pm 0.001) \times 10^{-2}$
cor[b)]	0.95×10^{-4}	$(0.172 \pm 0.001) \times 10^{-2}$
cor[b)]	3.89×10^{-4}	$(0.645 \pm 0.035) \times 10^{-2}$
cor[b)]	4.14×10^{-4}	$(0.637 \pm 0.031) \times 10^{-2}$
cor[b)]	9.97×10^{-4}	$(1.59 \pm 0.09) \times 10^{-2}$
cor[b)]	10.6×10^{-4}	$(1.58 \pm 0.01) \times 10^{-2}$
cor[b)]	14.3×10^{-4}	$(3.47 \pm 0.06) \times 10^{-2}$
cor[b)]	14.8×10^{-4}	$(3.10 \pm 0.02) \times 10^{-2}$
cor[b)]	19.7×10^{-4}	$(5.57 \pm 0.15) \times 10^{-2}$
cor[b)]	20.0×10^{-4}	$(5.91 \pm 0.12) \times 10^{-2}$
cor[b)b)]	28.5×10^{-4}	$(8.6 \pm 1.1) \times 10^{-2}$
cor[b)]	28.8×10^{-4}	$(7.40 \pm 0.74) \times 10^{-2}$
cor[b)]	29.2×10^{-4}	$(7.27 \pm 0.84) \times 10^{-2}$
str+cor[c)]	0.18×10^{9}	0.85 ± 0.18
str+cor[c)]	0.56×10^{9}	0.81 ± 0.10
str+cor[c)]	1.7×10^{9}	$0.61^{+0.08}_{-0.07}$
str+cor[c)]	5.5×10^{9}	$0.30^{+0.08}_{-0.07}$
str+cor[c)]	17×10^{9}	$0.42^{+0.14}_{-0.11}$
str+cor[c)]	0.5×10^{11}	<0.18
str+cor[c)]	1.7×10^{11}	<0.39
str+cor[d)]	1.8×10^{11}	<0.69
str+cor[d)]	5.6×10^{11}	<0.17
str+cor[d)]	18×10^{11}	<0.07
str+cor[d)]	56×10^{11}	<0.18
str+cor[e)]	1.4×10^{12}	96^{+60}_{-65}
str+cor[e)]	3.1×10^{12}	38^{+24}_{-22}
str+cor[e)]	14×10^{12}	6^{+8}_{-5}

Notes. Due to angular resolution limitations, in some cases the contributions from the starburst ring (str) and the AGN corona (cor) are disentangled. The messenger type of the data and associated references are as follows: [a)] γ: New data – see Sect. 3.1 for details. [b)] γ: Mutie et al. (2025). [c)] γ: Using a custom time coverage of J0242.6-0000 (NGC 1068) between 2008 and 2020 in the energy range 100 MeV−300 GeV taken from E+22. More details on the analysis can be found in Kun et al. (2022) and Kun et al. (2023). [d)] γ: Acciari et al. (2019). [e)] ν: Using three characteristic energies within the 68% confidence interval as reported by IceCube Collaboration (2022).

Table 4. Fit data for NGC 7469.

Env.	Energy [eV]	Flux [eV s^{-1} cm^{-2}]
str+cor[a)]	0.6×10^{-5}	$(1.68 \pm 0.07) \times 10^{-3}$
str+cor[b)]	2.0×10^{-5}	$(2.1 \pm 0.2) \times 10^{-3}$
str+cor[b)]	3.5×10^{-5}	$(2.63 \pm 0.03) \times 10^{-3}$
str+cor[b)]	9.3×10^{-5}	$(2.46 \pm 0.07) \times 10^{-3}$
str+cor[c)]	42×10^{-5}	$(5.0 \pm 0.5) \times 10^{-3}$
str+cor[c)]	46×10^{-5}	$(5.9 \pm 0.5) \times 10^{-3}$
cor[c)]	2×10^{-5}	$(0.84 \pm 0.08) \times 10^{-3}$
cor[c)]	4×10^{-5}	$(0.79 \pm 0.08) \times 10^{-3}$
cor[c)]	6×10^{-5}	$(0.65 \pm 0.06) \times 10^{-3}$
cor[c)]	14×10^{-5}	$(0.69 \pm 0.07) \times 10^{-3}$
cor[c)]	37×10^{-5}	$(1.8 \pm 0.2) \times 10^{-3}$
cor[c)]	41.7×10^{-5}	$(1.8 \pm 0.2) \times 10^{-3}$
cor[c)]	42.4×10^{-5}	$(1.7 \pm 0.2) \times 10^{-3}$
cor[c)]	46×10^{-5}	$(1.9 \pm 0.4) \times 10^{-3}$
cor[c)]	89×10^{-5}	$(5.0 \pm 0.5) \times 10^{-3}$
cor[c)]	95×10^{-5}	$(5.0 \pm 0.5) \times 10^{-3}$
cor[c)]	195×10^{-5}	$(37 \pm 20) \times 10^{-3}$
cor[c)]	198×10^{-5}	$(42 \pm 7) \times 10^{-3}$
cor[c)]	200×10^{-5}	$(41 \pm 20) \times 10^{-3}$
str+cor[d)]	0.2×10^{9}	<0.02
str+cor[d)]	0.6×10^{9}	<0.02
str+cor[d)]	1.8×10^{9}	<0.03
str+cor[d)]	5.6×10^{9}	<0.06
str+cor[d)]	17.8×10^{9}	<0.04
str+cor[d)]	56.2×10^{9}	<0.13
str+cor[d)]	178×10^{9}	<0.39
str+cor[d)]	562×10^{9}	<1.75
str+cor[e)]	1.61×10^{14}	(2.4 ± 1.4)

Notes. Due to angular resolution limitations, in some cases the contributions from the starburst ring (str) and the AGN corona (cor) are disentangled. The messenger type of the data and associated references are as follows: [a)] γ: New data – see Sect. 3.1 for details. [b)] γ: Taken from Clemens et al. (2008). [c)] γ: mm data retrieved from the ALMA archive (`https://almascience.nrao.edu/aq/`). [d)] γ: New data – see Sect. 3.1 for details. [e)] ν: Based on the average energy of the two neutrinos in the 90% confidence energy interval with an 68% confidence flux range of (0.007, 1.58) eV cm^{-2} s^{-1} from Abbasi et al. (2025).

extended diffuse component that is fixed from the given data at a few tens of gigahertz. However, this still leaves a huge variety of scenarios for the corresponding high-energy neutrino flux (transparent bright red lines in the right plot of Figs. 2 and 3), which all face some issues, as is discussed in more detail in the following.

4.1. NGC 1068

As is shown in Fig. 2, the updated Seyfert-starburst composite model is still able to explain the nonthermal observational data of NGC 1068. As found in E+22, the giga-electronvolt γ-rays originate from the starburst-ring, whereas with decreasing energy an increasing percentage of the observed sub-giga-electronvolt γ-rays result from the AGN corona. We noticed that the first Fermi-LAT data point[7] has a significant impact on the resulting solution, but at these energies the adopted spatial homogeneity also has a strong impact on the $\gamma\gamma$-pair attenuation as indicated by the dotted black line (that illustrates the result for a shield thickness of 5%). For most scenarios, the predicted neutrino flux is about a factor of two too small (but still partially within the uncertainty band) compared to the IceCube data. The overall spectral behavior between 1.4 and 14 TeV agrees quite well in many cases. Adopting an high-energy emission that is also surrounded by an isotropic X-ray target would enable an increased γ-ray and neutrino emissivity, leading to a better agreement with the IceCube data. Due to the comparably large uncertainties of the IceCube data, the neutrino flux predictions within the 1σ band of the best fit vary widely, whereas the millimeter flux

[7] From private communication with Emma Kun – more details can be found in Table 3.

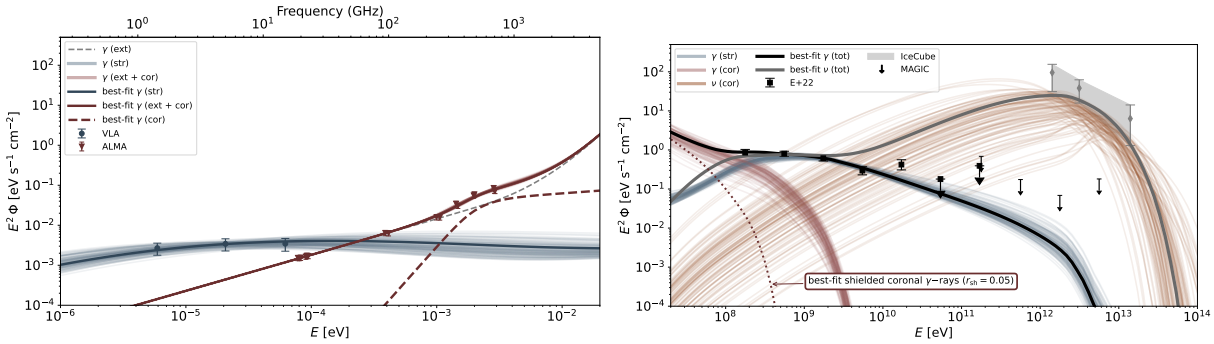


Fig. 2. Best-fit model prediction (and 100 alternative scenarios within 1σ of the best-fit in transparent colored lines) of the photon (γ) and neutrino (ν) SED of NGC 1068. The gray markers indicate characteristic neutrino flux values within the observed 68% confidence band that are used in the MCMC.

predictions hardly change. Therefore, we also investigated the case with an increased uncertainty of the millimeter data – by using a minimal uncertainty of $\gtrsim$30% – which reduces the need to obtain a coronal synchrotron bump at 100 GHz, so that a bump at slightly higher frequencies is sufficient. This enables higher values of ω_T – which shifts the characteristic synchrotron self-absorption frequency toward higher frequencies as systematically shown by del Palacio et al. (2025). Consequently, the target gas density needed for the neutrino production increases linearly and sufficiently small values of β_B ensure that the necessary CR proton energy for the high-energy neutrino production can still be reached. This leads to a perfect agreement with the IceCube data, as shown in Fig. B.1.

As shown by the posterior distributions (see Fig. A.1), all of the model parameters are close to the prior expectation. For the coronal radius, we obtain a rather distinct range of $\log(r_c) = 1.54 \pm 0.06$, which is in perfect agreement with the previous findings from Mutie et al. (2025).

4.2. NGC 7469

For the high-energy emission of NGC 7469, we first verified the basic result from Salvatore et al. (2025), showing that even a neutrino flux of $(32 \pm 16)\,\mathrm{eV\,s^{-1}\,cm^{-2}}$ at 161 TeV – based on using two associated neutrinos in 4 years of data (see Sommani et al. 2025) – can be explained by the AGN corona without overshooting the γ-ray upper limits (see Fig. B.2). Here, a small coronal radius of the order of a few Schwarzschild radii ($\mathcal{R}_s$) is needed. However, the millimeter data also introduce the need for a coronal contribution in the radio band, which is subsequently taken into account. The resulting best-fit scenario (see Fig. 3) indicates that this millimeter bump can be produced by the corona if it extends on scales of $>100\,\mathcal{R}_s$. But in that case there is no significant neutrino emission at some tens or hundreds of tera-electronvolts. So, a spatial homogeneous corona can either explain the millimeter bump or the observed hints for tera-electronvolt neutrinos, but not both. Note that even in the case of a minimal uncertainty of >30% the resulting best-fit scenario does not explain the current hints of high-energy neutrino emission due to the γ-ray constraints.

With respect to the starburst ring, our model can explain the large-scale radio emission and yields a giga-electronvolt γ-ray flux that is just about a factor of two below the current upper limits[8]. The associated posterior distributions (see Fig. A.2) indicate a spectral index of $s = -1.75 \pm 0.17$, which is significantly harder than the canonical expectation from standard DSA. Such a hardening may, in principle, arise in the high-energy part of the spectrum. For instance, nonlinear DSA predicts concave spectra that become increasingly hard at high energies due to shock modification by cosmic-ray pressure (Caprioli et al. 2010). Similarly, time-dependent effects related to the evolution of the remnant and the injection history can lead to additional hardening under specific assumptions, such as a constant injection number fraction (Drury 2011)[9]. Since the injected leptons are predominantly of hadronic origin, and therefore trace the high-energy proton population, such effects could provide a plausible explanation for the inferred hard spectrum, even though our simplified source term does not explicitly capture these spectral details.

Further, a slightly higher magnetic field strength as expected of $B_s > 10^{-3.7}$ G is needed to explain the large-scale radio data by synchrotron radiation from predominantly primary electrons. This results from the constrain on the maximal IC γ-ray emission, which yields an upper limit on the nonthermal electron density, and hence only leaves the magnetic field strength (apart from the spectral index of the CRs) to steer the primary synchrotron flux close to the data. All of the other parameters are in good agreement with the prior expectation.

5. Conclusions and discussion

In this work, we update the steady-state Seyfert-starburst composite model of E+22 with a more detailed treatment of its AGN corona:

(i) The interplay between SA and energy losses produces a significant hardening of the resulting nonthermal proton distribution.
(ii) Inclusion of the nonlinear secondary $e^{\pm}$ contribution, i.e., from leptonic radiation processes, which only becomes relevant, however, below a few hundred mega-electronvolts.
(iii) Inclusion of the $\gamma\gamma$-pair attenuation of the escaping γ-rays as well as a potential shielding scenario (where the X-ray corona is extended beyond the spatial scales of the γ-ray production site) has a strong impact on the resulting sub-giga-electronvolt γ-ray prediction if the radius of the X-ray corona is $\ll 100\,\mathcal{R}_s$.

Here, we assume a fixed magnetic turbulence spectrum and that the nonthermal particles extract only a negligible fraction of the turbulent energy, so that the turbulent cascade remains essentially unaffected. According to Lemoine et al. (2024) damp-

[8] In total the resulting sub-giga-electronvolt γ-ray flux is for most scenarios even less than a factor of two.

[9] In the more physically motivated case of self-regulated injection, these corrections largely cancel out, yielding a spectrum close to the standard DSA prediction.

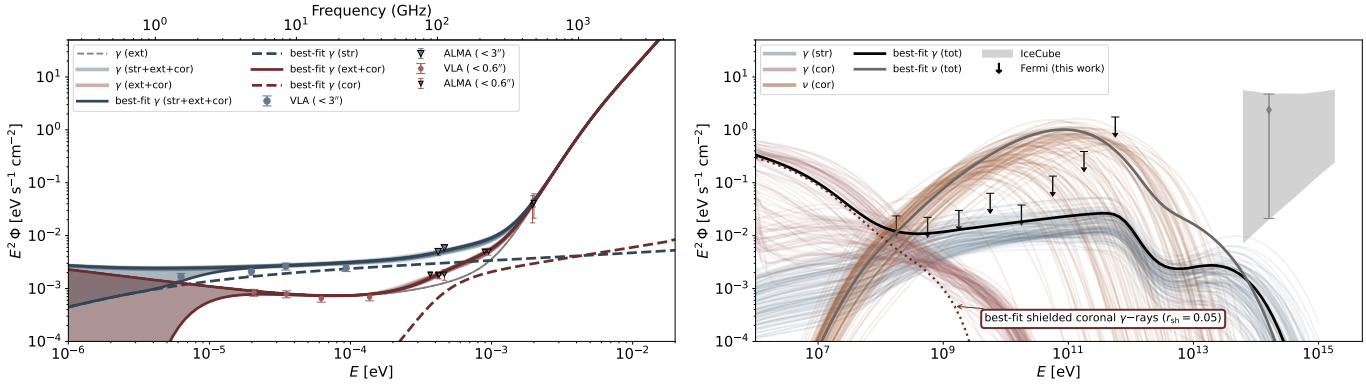


Fig. 3. Best-fit model predictions (and 100 alternative scenarios within 1σ of the best-fit in transparent colored lines) of the photon (γ) and neutrino (ν) SED of NGC 7469. The shaded blue and red bands at low energies refer to the uncertainty of the adopted extended gas distribution and its opacity with respect to free-free absorption. The gray markers indicate the characteristic neutrino flux value of the average energy (weighted with the signalness from Sommani et al. 2025) of the two neutrinos within the confidence band that is used in the MCMC.

ing is inefficient for $(v_A/c)^{q-1}\mathcal{E}_{nth}/\mathcal{E}_{B_0} \ll 1$, where $\mathcal{E}_{nth}/\mathcal{E}_{B_0}$ denotes the ratio of the total nonthermal particle energy density over the magnetic energy density. We verified that this condition is fulfilled for the given best-fit scenarios of NGC 1068 and NGC 7469. Note that if the turbulent cascade is not sufficiently powered externally the stochastic particle acceleration will become nonlinear and the resulting nonthermal particle energy spectrum will soften significantly at high energies, as has been shown by Lemoine et al. (2024), Lemoine & Rieger (2025).

We subsequently used an MCMC method to study the parameter space of the Seyfert-starburst composite galaxies NGC 1068 and NGC 7469. As in E+22, but with a more moderate CR pressure of about 0.1 P_{gas}, we are able to explain the multimessenger data of NGC 1068. However, a minor deficit (of about a factor of two) in the high-energy neutrino flux is obtained, if we explain the observed millimeter bump accurately. Since the likelihood is typically dominated by the radio data, we obtain in that case a uniform coronal radius of about $35\,\mathcal{R}_s$, which is in perfect agreement with the previous findings from Mutie et al. (2025). With respect to the neutrino deficit, it needs to be taken into account that the neutrino flux measurement adopts a power law with a best-fit spectral index of -3.2 ± 0.2. Using a different spectral behavior with a higher peak flux could decrease the observed flux above 1 TeV, as has been shown in Desai et al. (2025). Moreover, we took the coronal radio emission to emerge from the same spatial region such as the high-energy γ-ray and neutrino emission. But in principle, the confinement of charged particles depends on their Larmor radius; hence, the coronal radius for those particles that emit in the radio band could be much larger than the coronal radius at γ-ray energies. The MCMC results indicate that such a differentiation, whereby the radio corona is significantly larger than the γ-ray corona, would improve the fit to the data.

In the case of NGC 7469, the MCMC fits clearly indicate the need for a spatially inhomogeneous AGN corona: The millimeter bump needs to emerge from a coronal size of $R_c > 100\,\mathcal{R}_s$, whereas neutrino emission at energies >100 TeV requires $R_c < 10\,\mathcal{R}_s$ if there is no shielding outer photon target. A homogeneous corona with a fixed size at all energies can explain the features either at high energies or in the radio band, but not both. This discrepancy is generally known from other wave bands; for example, the sizes of the coronae inferred from X-rays are about $R_c \lesssim 10\,\mathcal{R}_s$ (Fabian et al. 2015), whereas the size of the millimeter emitter inferred via modeling of the SED yields sizes that are often larger, $R_c \sim (60\text{–}250)\,\mathcal{R}_s$ (del Palacio et al. 2025). We also note that the size discrepancy is too large to be explained just by time variability, with even the most extreme case of millimeter variability reported in Shablovinskaya et al. (2024) corresponding only to a change in size of about a factor of two.

Moreover, the predicted best-fit giga-electronvolt γ-ray flux of the starburst ring is just about a factor of two smaller than the current upper limits. In addition, a potentially dominant γ-ray contribution could emerge at sub-giga-electronvolt energies, where future observations will be able to draw further constraints.

Acknowledgements. BE and SS thank J. Dörner for fruitful discussion on the MCMC analysis as well as Emma Kun for the provided Fermi-LAT data analysis of NGC 1068. We acknowledge funding from the German Science Foundation DFG, within the Collaborative Research Center SFB1491 "Cosmic Interacting Matters – From Source to Signal". S.d.P. acknowledges support from ERC Advanced Grant 789410. We further thank Anna Franckowiak, Giacomo Principe, Filippo D'Ammando and Haocheng Zhang for constructive comments on the paper draft. The *Fermi* LAT Collaboration acknowledges generous ongoing support from a number of agencies and institutes that have supported both the development and the operation of the LAT as well as scientific data analysis. These include the National Aeronautics and Space Administration and the Department of Energy in the United States, the Commissariat à l'Energie Atomique and the Centre National de la Recherche Scientifique / Institut National de Physique Nucléaire et de Physique des Particules in France, the Agenzia Spaziale Italiana and the Istituto Nazionale di Fisica Nucleare in Italy, the Ministry of Education, Culture, Sports, Science and Technology (MEXT), High Energy Accelerator Research Organization (KEK) and Japan Aerospace Exploration Agency (JAXA) in Japan, and the K. A.Wallenberg Foundation, the Swedish Research Council and the Swedish National Space Board in Sweden. Additional support for science analysis during the operations phase is gratefully acknowledged from the Istituto Nazionale di Astrofisica in Italy and the Centre National d'Etudes Spatiales in France. This work is performed in part under DOE Contract DE-AC02-76SF00515. This paper makes use of the following ALMA data: ADS/JAO.ALMA#2017.1.00078.S, ADS/JAO.ALMA#2013.1.00218.S, ADS/JAO.ALMA#2013.1.00700.S. ALMA is a partnership of ESO (representing its member states), NSF (USA) and NINS (Japan), together with NRC (Canada), NSTC and ASIAA (Taiwan), and KASI (Republic of Korea), in cooperation with the Republic of Chile. The Joint ALMA Observatory is operated by ESO, AUI/NRAO and NAOJ.

References

Aartsen, M. G., Abbasi, R., Abdou, Y., et al. 2013, Phys. Rev. Lett., 111, 021103
Abbasi, R., Ackermann, M., Adams, J., et al. 2025, Evidence for Neutrino Emission from X-ray Bright Active Galactic Nuclei with IceCube
Abdollahi, S., Acero, F., Ackermann, M., et al. 2020, ApJS, 247, 33
Acciari, V. A., Ansoldi, S., Antonelli, L., et al. 2019, ApJ, 883, 135
Atwood, W. B., Abdo, A. A., Ackermann, M., et al. 2009, ApJ, 697, 1071
Beck, R. 2012, J. Phys.: Conf. Ser., 372, 012051

Blasi, P., & Amato, E. 2012, JCAP, 01, 010
Breit, G., & Wheeler, J. A. 1934, Phys. Rev., 46, 1087
Bruel, P., Burnett, T. H., Digel, S. W., et al. 2018, ArXiv e-prints [arXiv:1810.11394]
Caprioli, D., Amato, E., & Blasi, P. 2010, Astropart. Phys., 33, 160
Caprioli, D., Pop, A.-R., & Spitkovsky, A. 2014, ApJ, 798, L28
Clemens, M., Vega, O., Bressan, A., et al. 2008, A&A, 477, 95
del Palacio, S., Yang, C., Aalto, S., et al. 2025, A&A, 701, A41
Desai, A., Marchesi, S., Vandenbroucke, J., et al. 2025, ApJ, 993, 223
Drury, L. O. 2011, MNRAS, 415, 1807
Eichmann, B., Oikonomou, F., Salvatore, S., Dettmar, R.-J., & Tjus, J. B. 2022, ApJ, 939, 43
Fabian, A. C., Lohfink, A., Kara, E., et al. 2015, MNRAS, 451, 4375
Fiorillo, D. F. G., Comisso, L., Peretti, E., Petropoulou, M., & Sironi, L. 2024a, ApJ, 974, 75
Fiorillo, D. F. G., Petropoulou, M., Comisso, L., Peretti, E., & Sironi, L. 2024b, ApJ, 961, L14
Foreman-Mackey, D., Hogg, D. W., Lang, D., & Goodman, J. 2013, PASP, 125, 306
García-Burillo, S., Combes, F., Usero, A., et al. 2014, A&A, 567, A125
Gould, R. J. 1979, A&A, 76, 306
GRAVITY Collaboration (Pfuhl, O., et al.) 2020, A&A, 634, A1
Haggerty, C. C., & Caprioli, D. 2020, ApJ, 905, 1
Heitler, W. 1954, Quantum Theory of Radiation
Ho, L. C. 2008, ARA&A, 46, 475
Hopkins, P. F., Richards, G. T., & Hernquist, L. 2007, ApJ, 654, 731
Hsieh, P.-Y., Matsushita, S., Liu, G., et al. 2011, ApJ, 736, 129
IceCube Collaboration (Abbasi, R., et al.) 2022, Science, 378, 538
Inoue, Y., Khangulyan, D., & Doi, A. 2020, ApJ, 891, L33
Izumi, T., Kohno, K., Aalto, S., et al. 2015, ApJ, 811, 39
Jiang, Y.-F., Stone, J. M., & Davis, S. W. 2014, ApJ, 784, 169
Jiang, Y.-F., Blaes, O., Stone, J. M., & Davis, S. W. 2019, ApJ, 885, 144
Kheirandish, A., Murase, K., & Kimura, S. S. 2021, Astrophys. J., 922, 45
Kun, E., Jaroschewski, I., Ghorbanietemad, A., et al. 2022, ApJ, 940, 163
Kun, E., Bartos, I., Becker Tjus, J., et al. 2023, A&A, 679, A46
Laine, S., Kotilainen, J. K., Reunanen, J., Ryder, S. D., & Beck, R. 2006, AJ, 131, 701
Lemoine, M., & Rieger, F. 2025, A&A, 697, A124
Lemoine, M., Murase, K., & Rieger, F. 2024, Phys. Rev. D, 109, 063006
Marinucci, A., Bianchi, S., Matt, G., et al. 2016, MNRAS, 456, L94
Mehdipour, M., Kaastra, J., Costantini, E., et al. 2018, A&A, 615, A72
Merloni, A., & Fabian, A. C. 2001, MNRAS, 321, 549
Miller, K. A., & Stone, J. M. 2000, ApJ, 534, 398
Morlino, G., & Caprioli, L. 2012, A&A, 538, A81
Murase, K., Guetta, D., & Ahlers, M. 2016, Phys. Rev. Lett., 116, 071101
Murase, K., Kimura, S. S., & Mészáros, P. 2020, Phys. Rev. Lett., 125, 011101
Mutie, I. 2019, Master of Science by Research Thesis, The University of Manchester, Supervisors: Neal Jackson and Rob Beswick
Mutie, I. M., del Palacio, S., Beswick, R. J., et al. 2025, MNRAS, 539, 808
Petrosian, V., & Liu, S. 2004, ApJ, 610, 550
Ricci, C., Ho, L. C., Fabian, A. C., et al. 2018, MNRAS, 480, 1819
Salvatore, S., Eichmann, B., Sommani, G., et al. 2025, PoS, ICRC2025, 961
Shablovinskaya, E., Ricci, C., Kara, E., et al. 2024, A&A, 690, A232
Sommani, G., Franckowiak, A., Lincetto, M., & Dettmar, R.-J. 2025, ApJ, 981, 103
Strong, A. W., Moskalenko, I. V., & Ptuskin, V. S. 2007, Annu. Rev. Nucl. Part. Sci., 57, 285
Thompson, T. A., Quataert, E., Waxman, E., Murray, N., & Martin, C. L. 2006, ApJ, 645, 186
Trakhtenbrot, B., Ricci, C., Koss, M. J., et al. 2017, MNRAS, 470, 800
Veilleux, S., Cecil, G., & Bland-Hawthorn, J. 2005, ARA&A, 43, 769
Walter, D., & Eichmann, B. 2025, ApJ, 981, 22
White, R. L., Becker, R. H., Helfand, D. J., & Gregg, M. D. 1997, ApJ, 475, 479
Wood, M., Caputo, R., Charles, E., et al. 2017, Int. Cosm. Ray Conf., 301, 824
Wynn-Williams, C. G., Becklin, E. E., & Scoville, N. Z. 1985, ApJ, 297, 607
Yuan, Q., Zhang, B., & Bi, X.-J. 2011, Phys. Rev. D, 84, 043002

Appendix A: Posterior distributions

The Fig. A.1 show the posterior distribution of the analyzed parameter space of the starburst ring (first five parameter on the x-axis) and the AGN corona (second five parameters on the x-axis) of NGC 1068. The associated MCMC fit includes both environments, as they cannot be disentangled at high energies. The plot displays the results from 10000×30 iterations, whereof the first 1500 of each of the 30 walkers are due to correlation effects excluded, and only every 5th outcome is used.

In contrast to the previous case the MCMC fit of NGC 7469 has been performed for the AGN corona and the starburst ring separately, as there are currently only upper limits in the γ-ray band available. Therefore, the main contributions from those two environments can be nicely distinguished, if the high-energy neutrino hints emerge predominantly from the corona. Since the AGN corona model cannot explain the associated date, we only present the parameter analysis of the starburst ring (see Fig. A.2). Here, 15000×100 iterations have been performed, whereof only every fifth of the final 14000×100 iterations is used. In all MCMC runs we have verified that the calculations have converged.

Appendix B: Additional results

For comparison, we relax the observational constrain by the mm data in the likelihood by introducing a minimal relative uncertainty of 30%. This yields a perfect agreement with the high-energy neutrino data, as shown in Fig. B.1. The most striking difference in the associated fit parameters with respect to the ones from Fig. A.1, is a reduced coronal radius of about $28\,\mathcal{R}_s$ and an increased optical Thomson depth of 2. Hence, the production of high-energy neutrinos in a more compact, denser region within the X-ray corona could lead to a significant improvement of the fit.

For NGC 7469 we also tested to fit only the high-energy emission by the AGN corona. Here, we used only the upper limits on the gamma-ray flux as well as the neutrino flux indications at 161 TeV using the IceCube analysis given in Abbasi et al. (2025) (*left* plot in Fig. B.2) and the two-neutrino estimate from Sommani et al. (2025) (*right* plot in Fig. B.2), respectively. It is shown that that a perfect agreement with the hints for neutrino emission is possible, even in the case of the higher flux expectation from Sommani et al. (2025). But for this purpose the high-energy emission needs to emerge from an extremely compact coronal region of $\ll 10\,\mathcal{R}_s$. Note that due to the lack of observational constraints at high energies, the MCMC is strongly guided by the prior information leading to a huge number of predictions within the 1σ-regime of the best-fit scenario that, however, do not properly explain the observational hints for neutrino emission. Therefore, we decided to display only a few of those predictions with a posterior probability that deviates only marginally (i.e., $\ll 1\sigma$) from the best-fit.

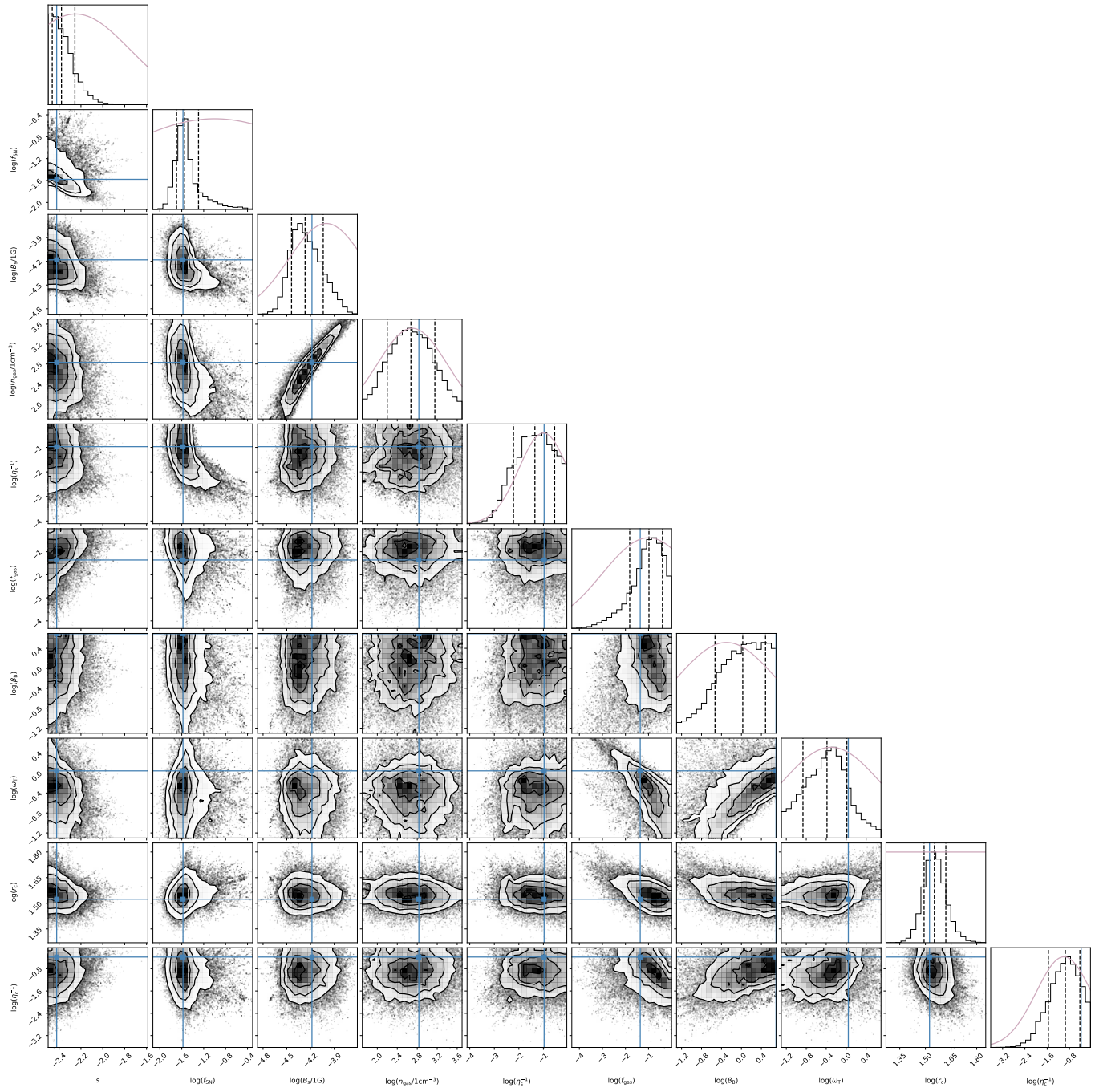


Fig. A.1. The posterior distribution of the fit parameters for NGC 1068. The blue lines indicate the best-fit parameter values and the magenta curve illustrates the adopted prior distribution.

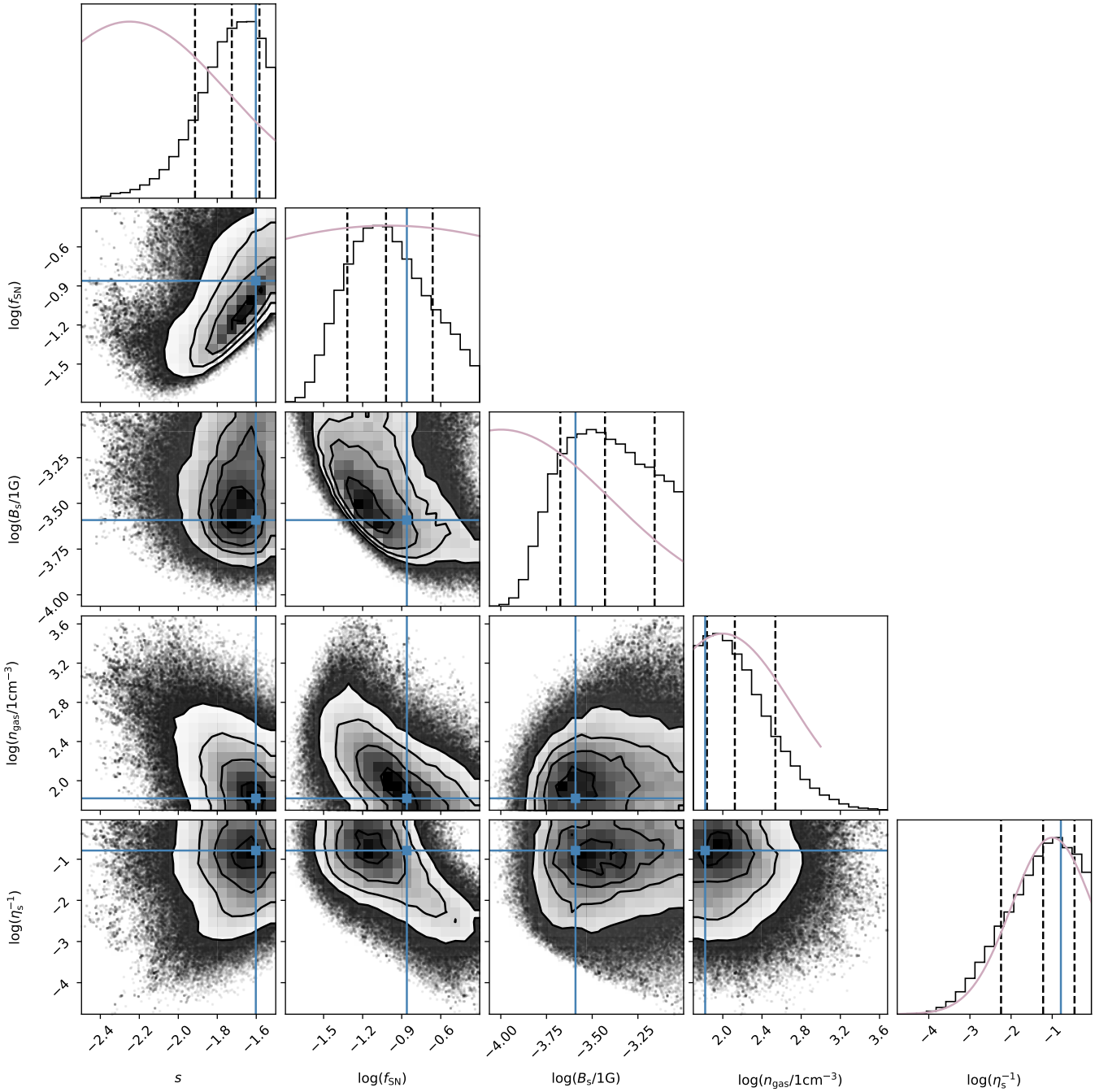


Fig. A.2. The posterior distribution of the fit parameters for the starburst ring of NGC 7469. The blue lines indicate the best-fit parameter values and the magenta curve illustrates the adopted prior distribution.

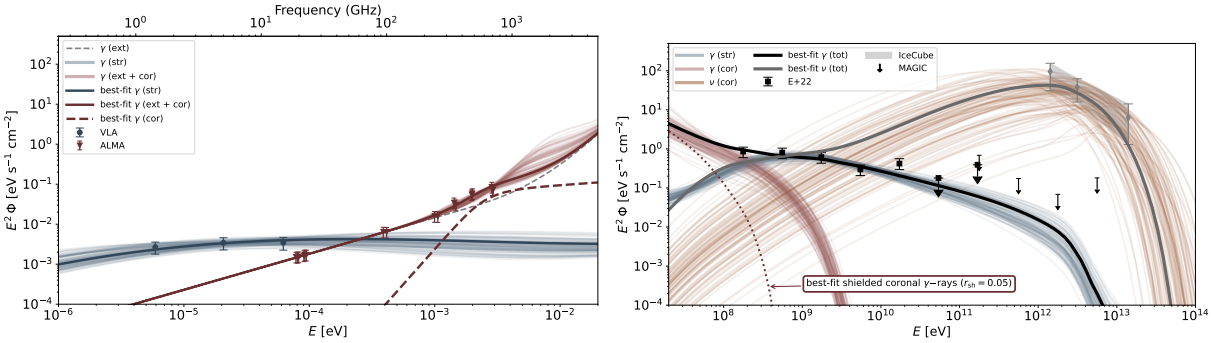


Fig. B.1. The best-fit model prediction (and 100 alternative scenarios within 1σ of the best-fit in transparent colored lines of the *photon (γ) and neutrino (ν)* SED of NGC 1068 assuming a minimal data uncertainty of 30 %. The gray markers indicate characteristic neutrino flux values within the observed 68% confidence band that are used in the MCMC.

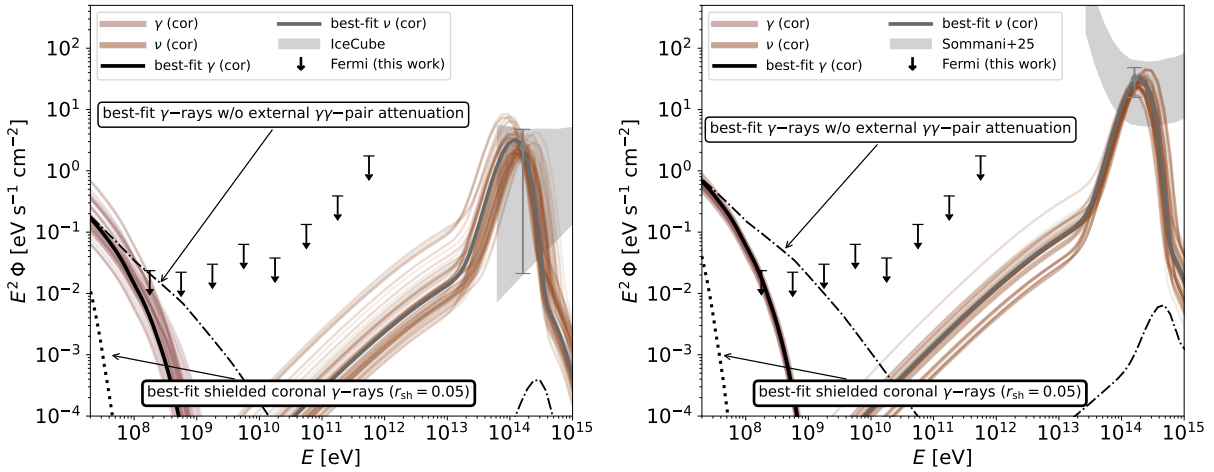


Fig. B.2. The best-fit model predictions (and 100 alternative predictions with only a marginally different posterior probability in transparent colored lines) of the coronal *photon (γ) and neutrino (ν)* SED of NGC 7469 at high energies considering only the γ-ray upper limits and the neutrino expectation from Abbasi et al. (2025) (*left*) and Sommani et al. (2025) (*right*), respectively. For the latter case (right), the 90% confidence interval (gray band) is converted to a 68% confidence value (gray marker) at the weighted average energy of 161 TeV, which yields $(32 \pm 16)\,\mathrm{eV\,cm^{-2}\,s^{-1}}$ for 4 years of data and two associated muon neutrinos.